



# Effects of post-weld heat treatment on microstructure and mechanical properties of the welded joints by using multi-principal filler materials

Dejia Liu<sup>1,2</sup> · Chongling Ni<sup>1</sup> · Xuean Zha<sup>1</sup> · Longzhi Zhao<sup>1,2</sup> · Yu Sun<sup>3</sup>

Received: 22 February 2023 / Accepted: 5 April 2023 / Published online: 22 April 2023  
© International Institute of Welding 2023

## Abstract

Two types of multi-principal filler materials of FeCoCrNiMn and CrNi<sub>2</sub>MnTi<sub>0.5</sub>Al<sub>0.5</sub> powders were used to butt weld the 304/Q235 stainless steel composite plate. The effects of post-weld heat treatment (PWHT) on the grain morphologies, phase structures, microhardness, and tensile properties of two welded joints were explored and discussed. An interesting finding was that the PWHT process had markedly different effects on the hardness, tensile properties, and fracture behavior of two welded joints. A simple phase structure, a face-centered cubic (FCC) phase, was achieved in the weld metal by using FeCoCrNiMn powders. The PWHT process had small effects on the microstructure, hardness value, tensile strength, and fracture position of the FeCoCrNiMn sample. However, the PWHT process could sharply increase the hardness and significantly decrease the tensile strength of the CrNi<sub>2</sub>MnTi<sub>0.5</sub>Al<sub>0.5</sub> sample. Moreover, the grain morphologies in the weld zone were changed from columnar/equiaxed grains into structures with irregular morphologies for the CrNi<sub>2</sub>MnTi<sub>0.5</sub>Al<sub>0.5</sub> sample after the PWHT process.

**Keywords** Post-weld heat treatment · Stainless steel composite plate · Multi-principal filler materials · Microstructure · Tensile properties · Hardness

Recommended for publication by Commission II - Arc Welding and Filler Metals.

## Highlights

- Two types of multi-principal filler materials were used to butt weld the 304/Q235 stainless steel composite plate.
- The effects of post-weld heat treatment (PWHT) on the microstructure and mechanical properties of two welded joints were explored.
- The PWHT process had different effects on the hardness variation and tensile properties of two welded joints.
- The PWHT process could sharply increase the hardness, and decrease the tensile strength of the CrNi<sub>2</sub>MnTi<sub>0.5</sub>Al<sub>0.5</sub> sample.

✉ Dejia Liu  
ldj515@126.com

✉ Yu Sun  
sunyu@chinansc.cn

<sup>1</sup> School of Materials Science and Engineering, East China Jiaotong University, ShuangGang East Street 808#, Economic and Technological Development Zone, Nanchang, China

<sup>2</sup> State Key Laboratory of Performance Monitoring Protecting of Rail Transit Infrastructure, Nanchang, China

<sup>3</sup> Nuclear and Radiation Safety Center, Ministry of Ecology and Environment, Beijing, China

## 1 Introduction

High-entropy alloys (HEAs) are composed of five or more principal elements, with the concentration of each element being between 5 and 35 at.% [1]. Compared to traditional alloys, HEAs present four main characteristics [2–4], including the cocktail effect, sluggish diffusion effect in dynamics [5], the high-entropy effect in thermodynamics, and the severe lattice distortion effect in structure [6]. HEAs are prone to achieve superior performance, including high strength, toughness, and corrosion resistance [7–9]. The weldability of HEAs has been widely studied in previous studies [10–15]. Moreover, using HEAs as filler material in welding to improve weld formation and mechanical characterization of welded joints has practical application promise [7]. According to past research, some academics have used HEAs as filler materials in the welding process [16–22]. For example, the filler material of (FeCoCrNi)<sub>100-x</sub>Cu<sub>x</sub> was used to achieve the joining of TC4 alloy and 304 stainless steel [22]. It has been reported that with an increase of Cu content in filler material, the amount and size of segregated Cu-rich phases were significantly increased in the weld zone (WZ). The tensile strength of the joint with

CoCrFeNi filler material was 158 MPa, and it decreased with an increase of Cu in the filler material until the atomic percent of Cu reached 27.27 at.%, but raised to 161 MPa by using (CoCrFeNi)<sub>66.67</sub>Cu<sub>33.33</sub> filler material [22]. The reason may be closely related to the changes in the phase structure and content of the WZ [22]. Zheng et al. [23] have studied the interfacial microstructure and strengthening mechanism of the dissimilar metal joint of Al/steel via a porous HEA coating. A multi-principal filler material of Ni-Mn-Fe-Co-Cu was employed to create a laser-brazed Inconel 718 joint [24]. The shear strength of 220 MPa was obtained [24]. Moreover, a recent study found that the production of Fe-Al IMCs in the WZs of Al/steel joints was considerably inhibited by using multi-principal filler materials of CoZnCuMn<sub>0.8</sub>Si<sub>0.2</sub> and FeCoCrNiMn [16]. Therefore, it is meaningful to use multi-principal filler materials via a high-entropy design to enhance the welding quality.

Heat treatment is an effective and common method to modify the microstructure and mechanical properties of alloys [25–27]. For many HEAs, owing to their promising thermal stability, the phase structure remains almost unchanged under heat treatment at 650~1100 °C [28–31]. A study has reported that a single FCC solid solution is always observed before and after heat treatment at 500 °C, 900 °C, and 1100 °C for the FeCoCrNiMn alloy [32]. On the contrary, some other scholars have reported that the phase structures and mechanical properties of HEAs can be changed during heat treatment. For instance, it is reported that a new FCC phase is generated in the AlCoCuFeMnNi alloy after the heat treatment at 900 °C, which causes the yield strength (YS) to decrease from 1833 ± 45 to 1095 ± 45 MPa. And the hard phase  $\sigma$  can be dissolved, and the content of the body-centered cubic (BCC) phase is reduced when the temperature reaches 700~800 °C for the cast FeCrCuMnNi alloy [33, 34]. Therefore, the effects of heat treatment on the phase composition, microstructure, and mechanical properties of HEAs seem to be controversial. It may have a close relationship with the heat treatment conditions and chemical composition of HEAs.

Post-weld heat treatment (PWHT) is a common method to improve the service properties of welded joints. Nam et al. [35] reported that for the welded joints of CoCrFeMnNi alloy, an FCC solid-solution structure is observed in the WZ regardless of how the PWHT temperature varies. And the grain size is increased, which leads to a slight reduction in the hardness and strength of the WZ [35]. However, the effect of PWHT on the microstructure and mechanical properties of the welded joints, using multi-principal filler materials with a high-entropy design, has been rarely studied. As is known, owing to their excellent corrosion resistance and low price, 304/Q235 stainless steel clad sheets are commonly used in the fields of the chemical industry, navigation, and petroleum vessels. At present, sequentially

layered-to-layered welding of the base plate, interlayer, and flyer plate of stainless steel clad sheets, using various filler materials, is widely adopted to ensure the mechanical properties and corrosion resistance of the weld metal. It may be possible to achieve the excellent joint performance of the stainless steel-clad sheets by using high-entropy alloys as a single filler material. In the present study, two types of multi-principal filler materials of FeCoCrNiMn and CrNi<sub>2</sub>MnTi<sub>0.5</sub>Al<sub>0.5</sub> were designed. 304/Q235 stainless steel composite plate was butt-welded by using multi-principal filler materials. The effects of PWHT on the phase structures, grain morphologies, microhardness, and tensile properties of two welded joints were explored and discussed.

## 2 Materials and methods

The base metal (BM) used in this study was 304/Q235 stainless steel composite plates (including the 1 mm 304 flyer layer and 2 mm Q235 base layer), which were produced by explosive welding. Two types of multi-principal filler materials were used, including FeCoCrNiMn and CrNi<sub>2</sub>MnTi<sub>0.5</sub>Al<sub>0.5</sub> powders. As is known, the fabrication of the HEA welding rod or wire is complicated, which is not conducive to the early exploration of filler materials using HEAs. Laser powder welding is suitable for the design and optimization of high-entropy filler materials. The commercial and equiatomic FeCoCrNiMn HEA powders were utilized as one type of filler material. The other type of filler material was designed based on the FeCoCrNiMn alloy and without the Co element. In this filler material, the Co element was replaced by the Ni element, and two elements of Ti and Al were used to replace the Fe element. Therefore, the filler material was fabricated by using Cr, Ni, Mn, Ti, and Al elemental powders with a purity of 99.99 wt.%. The five elements were mixed with a notional Cr: Ni: Mn: Ti: Al molar ratio of 1: 2: 1: 0.5: 0.5. It was named the CrNi<sub>2</sub>MnTi<sub>0.5</sub>Al<sub>0.5</sub> powders. It means the mass ratio of Cr: Ni: Mn: Ti: Al = 19.86 wt. %: 44.85 wt. %: 22.99 wt. %: 9.15 wt. %: 5.15 wt. %. Those elemental powders with the size of 140~300  $\mu$ m were well mixed and then dried in a vacuum oven.

Owing to the welding mode of heat conduction, deep penetration welding is hardly achieved in laser powder welding. To achieve full penetration in welding and reduce the weld metal dilution, the 304/Q235 stainless steel composite plate had a 60° X-groove. Using the LDM2500-60 semiconductor laser and K1000M4i-A numerical control system, the stainless steel composite plates were welded by a continuous laser beam via two pass using coaxial powder feeding. As is known, the welding parameter is an important factor affecting the results. A low welding heat input may cause some filler metal powders not to

melt. The high welding heat input may melt excessive BM, which results in severe weld metal dilution. Therefore, the welding heat input used in the study should be able to completely melt filler metal powders and decrease the weld metal dilution to the greatest extent. After optimizing the welding parameters, a set of welding parameters was selected. A laser power of 1400 W was used. The welding speed was 250 mm/min. The flow rate of the protective gas was 15 L/min. The rate of powder feeding was 16 g/min. A 1.5 mm assembly gap between the two workpieces was applied. The welded joints obtained by using FeCoCrNiMn and CrNi<sub>2</sub>MnTi<sub>0.5</sub>Al<sub>0.5</sub> powders were named as FeCoCrNiMn and CrNi<sub>2</sub>MnTi<sub>0.5</sub>Al<sub>0.5</sub> samples, respectively. It has been reported that the phase structure and composition have good stability at high temperatures for most HEAs. For the FeCoCrNiMn alloy, the annealing temperature of 700~1200 °C was usually selected. Therefore, some of those samples were subjected to PWHT at 800 °C for 4 h by the electric box-type heating furnace (SXL-1200C, Shanghai Jujing, China) in the present study. And those samples were named as FeCoCrNiMn PWHT and CrNi<sub>2</sub>MnTi<sub>0.5</sub>Al<sub>0.5</sub> PWHT samples, respectively.

Metallographic samples were prepared from the cross-sections of the welded joints before and after the PWHT. The electro-discharge cutting was selected to obtain the required metallographic samples. To observe the microstructures, the specimens were grounded and polished to a mirror-smooth finish. The microstructures on the Q235 layer were etched by using a 4% nitric acid alcohol solution for 20 s. Then, those were etched with aqua regia for 10 s to observe the microstructures in the 304 stainless steel layer, as well as the weld metal. The microstructures and element distribution were studied using Zeiss Axio Vert.A1 optical microscopy (OM), Hitachi SU8010 scanning electron microscope (SEM), and Bruker Xflash 6I60 energy dispersive spectrometer (EDS). The phase structures in various samples were investigated by the D8-ADVANCE X-ray diffraction (XRD, Bruker, USA), using a Shimadzu XRD-6100 X-ray diffractometer with a Cu K $\alpha$  target. The scan speed was 2° per minute. The scanned range of 2 $\theta$  was from 30 to 90°. The hardness values of those samples were achieved by using a Vickers microhardness tester (HV1000IS, Jujing, China). The hardness testing standard of GB/T 4340–2009, which is the same as the standard ISO 6507:2005, was used. The holding time was 10 s with a loading force of 200 g. Standard dumbbell tensile samples (26 mm gauge length, 10×3 mm cross-section) were manufactured. All surfaces of the tensile specimens were polished to reduce surface roughness before the tensile tests. The transverse tensile tests were conducted at room temperature with a strain rate of 1×10<sup>-3</sup>/s. The tensile test procedure was conducted according to GB/T 228.1–2021. To achieve the reliability of experimental results, tensile tests for each type of sample were repeated three times.

## 3 Results

### 3.1 Microhardness

The hardness distributions on the cross-section of various samples are presented in Fig. 1. The hardness value of the 304 BM (240~250 HV) is higher than that of the Q235 BM (~120 HV). For the FeCoCrNiMn sample, the average hardness in the WZ is ~180 HV, which is ~70% of that of the 304 BM and 1.5 times larger than that of the Q235 BM. Therefore, a “W” shape is seen in the hardness curve of the 304 layer (Fig. 1a), while an “M” shape is observed on the Q235 layer (Fig. 1b). It means that the hardness of the WZ using FeCoCrNiMn powders is located at intermediate values between 304 BM and Q235 BM. Based on the positive relationship between hardness and strength, it may indicate that the strength of the WZ should be lower than that of the 304 layer and higher than that of the Q235 layer. This may coordinate the deformation of those two layers during the tensile tests and have an impact on the tensile strength and fracture position of the FeCoCrNiMn sample. Moreover, for the FeCoCrNiMn PWHT sample, Fig. 1a and b indicate that the hardness values in the WZ are slightly decreased to 160~170 HV. It should be stated that the effect of PWHT on the hardness of the WZ for the FeCoCrNiMn sample is similar to the previous studies on the heat treatment of FeCoCrNiMn alloy [36–39]. It was reported that the hardness of the FeCoCrNiMn alloy is almost unchanged after heat treatment at 500 °C, with a value of ~200 HV. As the heat treatment temperature increased to 1100 °C, the hardness value slightly decreased to ~180 HV, owing to the grain coarsening after heat treatment [31]. Nam et al. [35] discovered that when the heat treatment temperature was 800 °C, little change in hardness could be found in the welded joints of FeCoCrNiMn alloys.

Figure 1c and d indicate that for the CrNi<sub>2</sub>MnTi<sub>0.5</sub>Al<sub>0.5</sub> sample, the hardness values in the WZ (210~220 HV) are slightly lower than that of the 304 BM and higher than the Q235 BM. However, after the PWHT, the hardness values in the WZ sharply increase to 340~380 HV on the 304 layer, and those are 380~470 HV on the Q235 layer. Moreover, Fig. 1c shows that for the CrNi<sub>2</sub>MnTi<sub>0.5</sub>Al<sub>0.5</sub> PWHT sample, the hardness value of the weld edge (370~390 HV) is higher than that of the weld center (~340 HV) on the 304 layer, while the hardness of the weld edge is lower than that of the weld center on the Q235 layer (Fig. 1d). It means that significant hardness variation is presented in the WZ of the CrNi<sub>2</sub>MnTi<sub>0.5</sub>Al<sub>0.5</sub> PWHT sample. The results should be related to the differences in elemental content and microstructure between the weld edge and the weld center. Based on previous studies [18, 19], owing

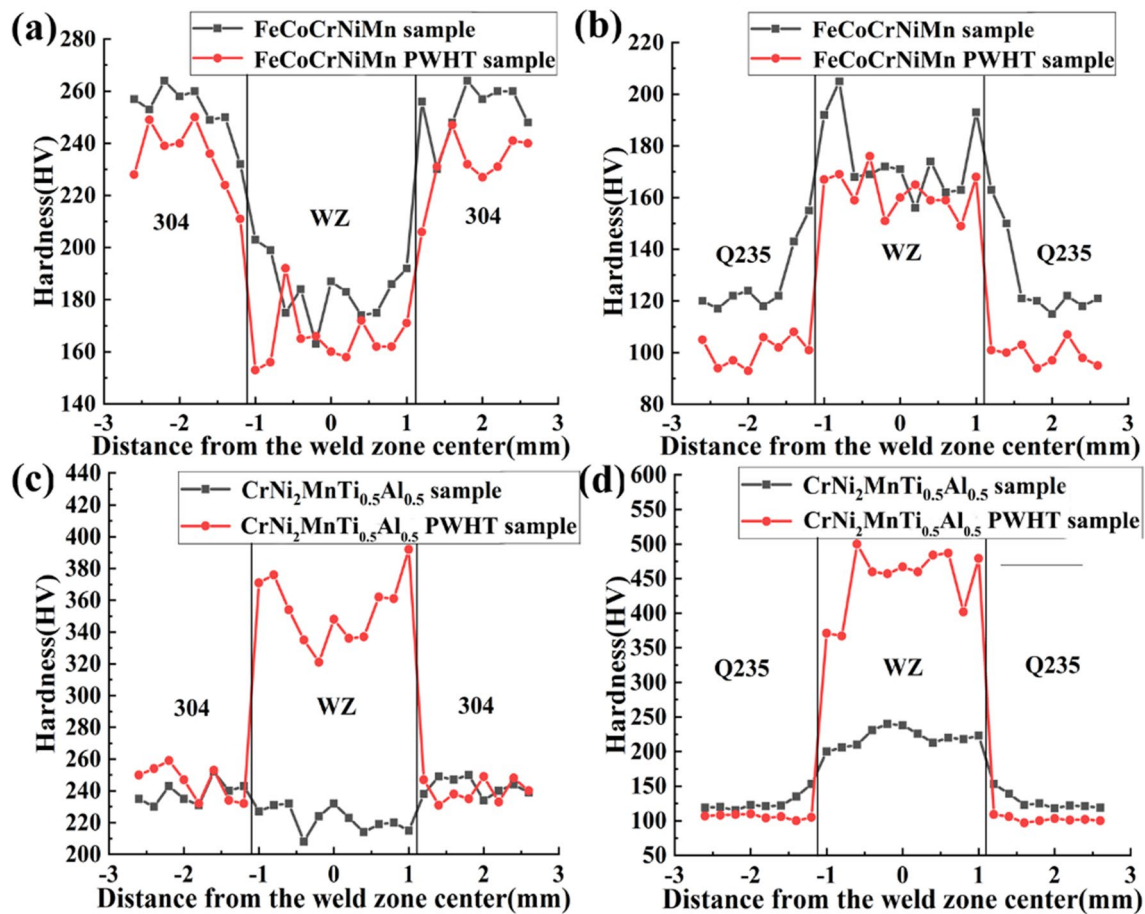


**Fig. 1** Microhardness distribution of various samples: **a, b** FeCoCrNiMn samples; **c, d** CrNi<sub>2</sub>MnTi<sub>0.5</sub>Al<sub>0.5</sub> samples; **a, c** 304 layer; **b, d** Q235 layer

to the melting of the BM and weld metal dilution during laser powder welding, chemical composition inhomogeneity, and non-uniform microstructure are easily presented in the WZ, especially for the composite plate.

An interesting finding is observed for the hardness variation of the WZs for the FeCoCrNiMn and CrNi<sub>2</sub>MnTi<sub>0.5</sub>Al<sub>0.5</sub> samples after the PWHT. The hardness of the former is slightly decreased, while that of the latter is sharply increased after PWHT. It may be closely related to the microstructure and phase transformation of two welded joints during the PWHT process. It also may have an impact on the tensile properties of those two types of welded joints.

### 3.2 Tensile properties

Figure 2a reveals the tensile properties of the FeCoCrNiMn samples. The ultimate tensile strength (UTS) and YS of the FeCoCrNiMn sample are  $518.3 \pm 10$  MPa and  $420.5 \pm 15$  MPa, respectively. And those of the FeCoCrNiMn PWHT sample are  $545.8 \pm 18$  MPa and  $325.6 \pm 20$  MPa, respectively. It means that for the

FeCoCrNiMn samples, the PWHT process has a small effect on the tensile properties, including a slight increase in the UTS and a decrease in the YS. Moreover, the inset of Fig. 2a indicates that the FeCoCrNiMn samples before and after the PWHT are fractured in the BM region, which is about 6–8 mm away from the WZ. It means that the weld metal shows better mechanical properties than the BM. The tensile properties of the FeCoCrNiMn samples have not deteriorated during the PWHT. The fracture position for the tensile samples has not changed during the PWHT for the welded joints using FeCoCrNiMn multi-principal filler material. The results are similar to some previous studies about the welded joints of FeCrCoNiMn alloy [37, 40–42]. Tong et al. [32] found that the tensile strength of FeCrCoMnNi alloy hardly changes after the heat treatment at 700 °C or 1100 °C. Nam et al. [35] reported that the UTS of the laser-welded joint of FeCrCoMnNi alloy would be slightly decreased from ~650 to ~600 MPa after the PWHT at 800–1000 °C. The decrease in grain size and the fraction of CrMn-oxide inclusions are attributed to the results [35].

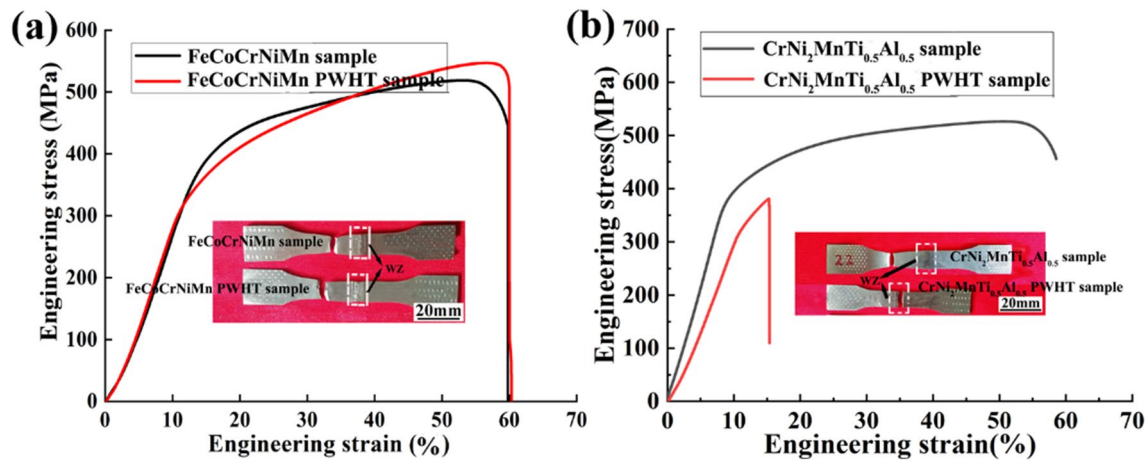


**Fig. 2** Strain–stress curve and fracture location of two types of welded joints before and after the PWHT: **a** FeCoCrNiMn samples; **b** CrNi<sub>2</sub>MnTi<sub>0.5</sub>Al<sub>0.5</sub> samples

Figure 2b indicates that for the CrNi<sub>2</sub>MnTi<sub>0.5</sub>Al<sub>0.5</sub> sample, the UTS is  $526 \pm 14$  MPa and the YS is  $343 \pm 9$  MPa. However, for the CrNi<sub>2</sub>MnTi<sub>0.5</sub>Al<sub>0.5</sub> PWHT sample, the UTS is significantly decreased to  $380 \pm 22$  MPa. The elongation is markedly decreased compared to the CrNi<sub>2</sub>MnTi<sub>0.5</sub>Al<sub>0.5</sub> sample. The inset of Fig. 2b reveals that the CrNi<sub>2</sub>MnTi<sub>0.5</sub>Al<sub>0.5</sub> sample is fractured in the BM.

However, for the CrNi<sub>2</sub>MnTi<sub>0.5</sub>Al<sub>0.5</sub> PWHT sample, it is fractured in the WZ. It means that the fracture position of the CrNi<sub>2</sub>MnTi<sub>0.5</sub>Al<sub>0.5</sub> samples has significantly changed after the PWHT. Therefore, an interesting finding is that the PWHT process harms the tensile properties and changes the fracture position of those two CrNi<sub>2</sub>MnTi<sub>0.5</sub>Al<sub>0.5</sub> samples. The fracture morphologies of the CrNi<sub>2</sub>MnTi<sub>0.5</sub>Al<sub>0.5</sub>

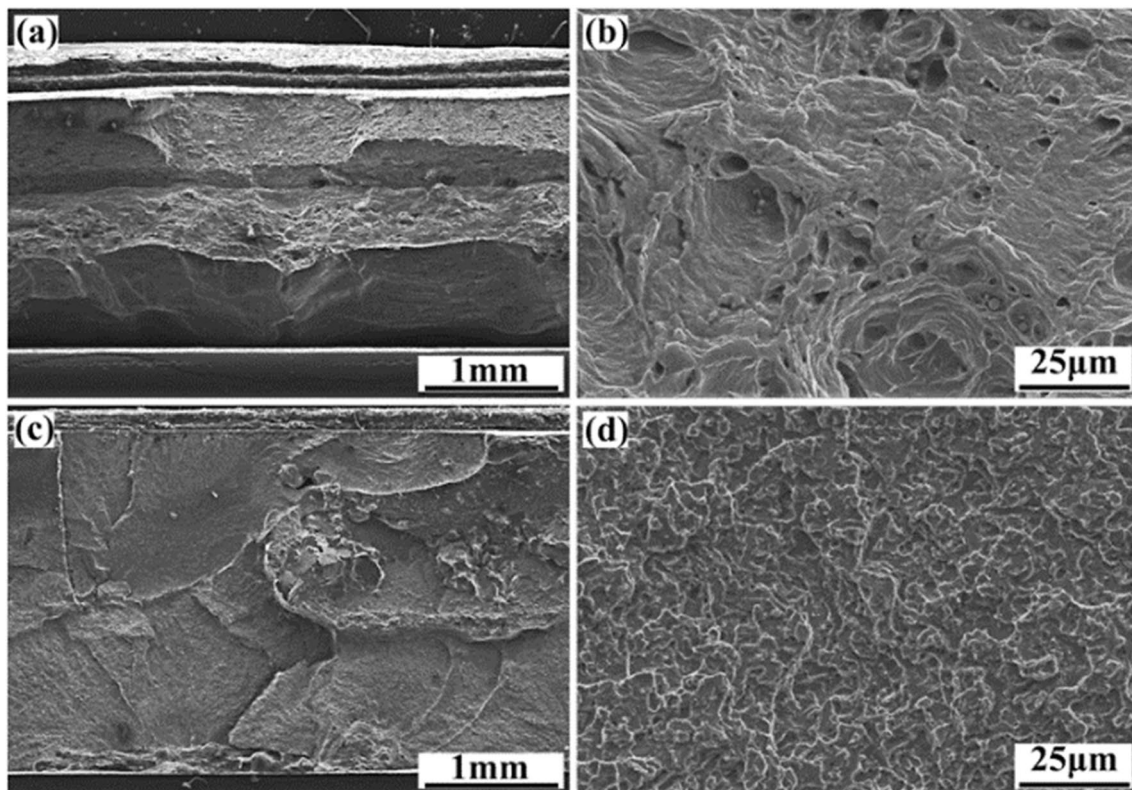


**Fig. 3** Fracture morphologies of the tensile CrNi<sub>2</sub>MnTi<sub>0.5</sub>Al<sub>0.5</sub> samples: **a, b** before the PWHT; **c, d** after the PWHT

samples are presented in Fig. 3. Large and deep dimples can be observed in the  $\text{CrNi}_2\text{MnTi}_{0.5}\text{Al}_{0.5}$  sample. It confirms a ductile fracture in the 304/Q235 stainless steel composite plate because the  $\text{CrNi}_2\text{MnTi}_{0.5}\text{Al}_{0.5}$  sample is fractured in the BM. However, for the  $\text{CrNi}_2\text{MnTi}_{0.5}\text{Al}_{0.5}$  PWHT sample, Fig. 3d shows obvious cleavage steps on the fracture surface. It is well consistent with the decreased elongation of the sample compared to the  $\text{CrNi}_2\text{MnTi}_{0.5}\text{Al}_{0.5}$  sample (Fig. 2b). Those results indicate that the PWHT process has markedly different effects on the tensile properties and fracture behavior of the welded joints by using multi-principal filler materials of FeCoCrNiMn and  $\text{CrNi}_2\text{MnTi}_{0.5}\text{Al}_{0.5}$ . The findings could be related to the variation of element distribution, grain morphologies, grain size, and phase structures during the PWHT process.

### 3.3 Microstructure evolution

The microstructure evolution in the WZ of the FeCoCrNiMn sample can be observed on the low-magnification image of Fig. 4a. Columnar grains can be observed in the weld edge, as shown in Fig. 4b. Cellular crystals can be seen in the region which is close to the weld center (Fig. 4c). Previous studies have reported a similar observation in the laser-manufactured or welded FeCoCrNiMn alloy [42–46]. The formation of the grain morphology is due to the solidification effects during fusion welding [47]. Tong et al. [32] suggested

that the formation of columnar grains in the weld edge is mainly due to the large temperature gradient in the molten pool during the laser forming process, which promotes the growth of columnar crystals along the gradient direction. As the region is nearing the weld center, a relatively low temperature gradient and cooling rate hinder the growth of columnar crystals. Comparing the grain structures of the FeCoCrNiMn samples before and after PWHT (Fig. 4b–e), no significant changes have occurred in the grain morphologies of the WZ. Slight grain growth can be found in the WZ of the FeCoCrNiMn sample after PWHT, comparing the columnar grains in Fig. 4b and d. As indicated in Fig. 4f, the elements in the WZ of the FeCoCrNiMn sample are uniformly distributed. No segregation of elements is observed. Based on the experimental results, the content of each element in the tested region of the WZ is Fe: Co: Cr: Ni: Mn = 25.2 at.%: 13.3 at.%: 23.2 at.%: 18.8 at.%: 19.5 at.%. This is in line with the definition of HEAs with elemental content of 5–35 at.%.

Figure 5a and b show the microstructures in the WZs of the  $\text{CrNi}_2\text{MnTi}_{0.5}\text{Al}_{0.5}$  samples. Typical columnar grains with the primary arm spacing of  $5.8 \pm 0.9 \mu\text{m}$  are observed adjacent to the weld edge. Equiaxed grains with an average grain size of  $9.1 \pm 1.5 \mu\text{m}$  are found in the weld center. Moreover, many white particles are distributed in the grain boundaries or within the grains (Fig. 5a, b). To further analyze the chemical composition of the particles and

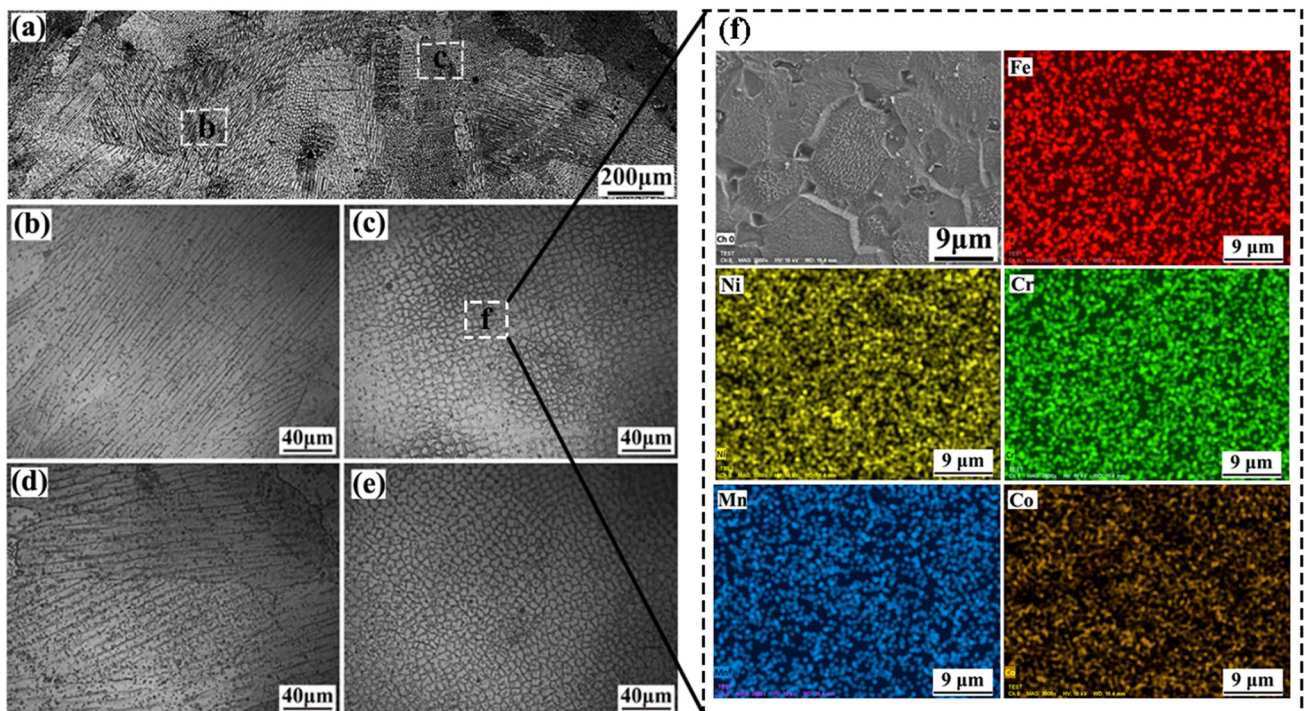


**Fig. 4** Microstructure in WZ of the FeCoCrNiMn samples: **a** low-magnification image of the WZ; **b**, **d** weld edge; **c**, **e** weld center; **b**, **c** before the PWHT; **d**, **e** after the PWHT; **f** element surface distribution in the WZ of the FeCoCrNiMn sample

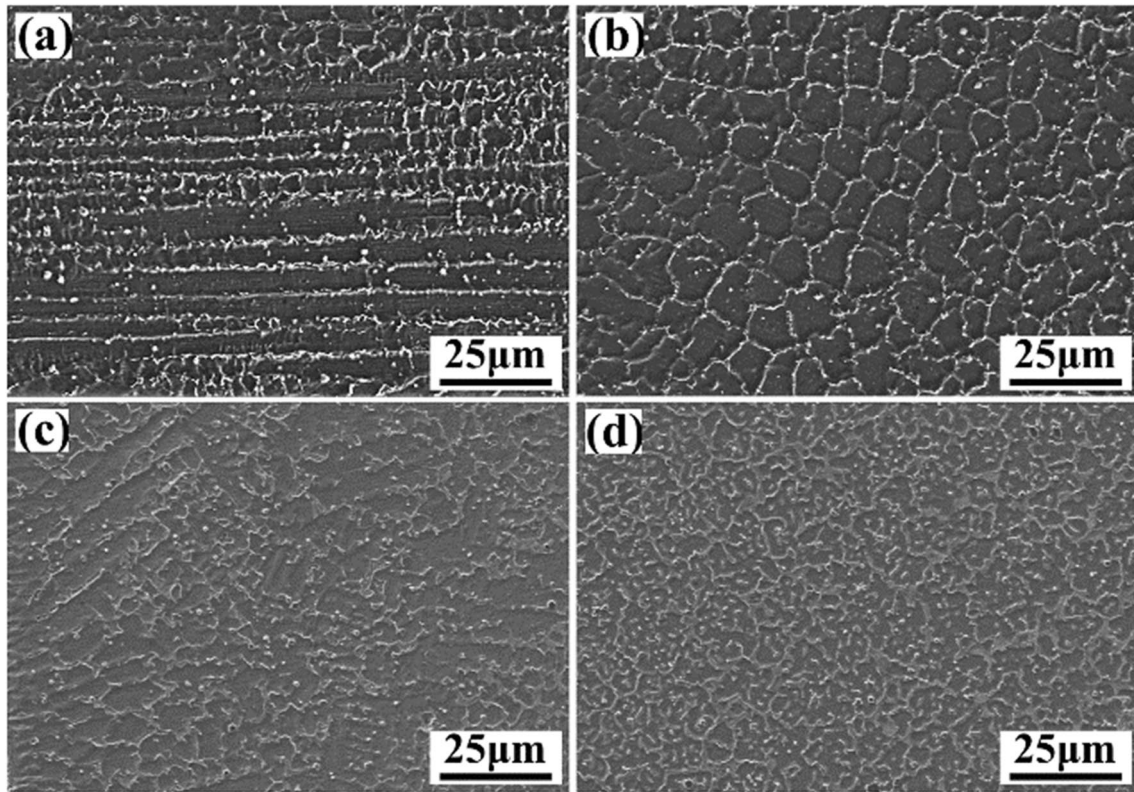


**Fig. 5** Microstructure in WZ of the CrNi<sub>2</sub>MnTi<sub>0.5</sub>Al<sub>0.5</sub> samples: **a, c** the weld edge; **b, d** the weld center; **a, b** before the PWHT; **c, d** after the PWHT

the matrix in the WZ of the CrNi<sub>2</sub>MnTi<sub>0.5</sub>Al<sub>0.5</sub> sample, EDS elemental mapping for the region showing equiaxed grains is provided in Fig. 6a. It is observed that Ti and Al elements are aggregated near the particles, as shown by the white arrow in Fig. 6a. The results indicate that

the particles may be Ti–Al-rich particles. Moreover, EDS point analysis was used to evaluate the elemental content of the characteristic points of the matrix (A-point) and the particles (B-point). The results can be found in the inset of Fig. 6a. A high content of Fe element (~ 61 at.%) is

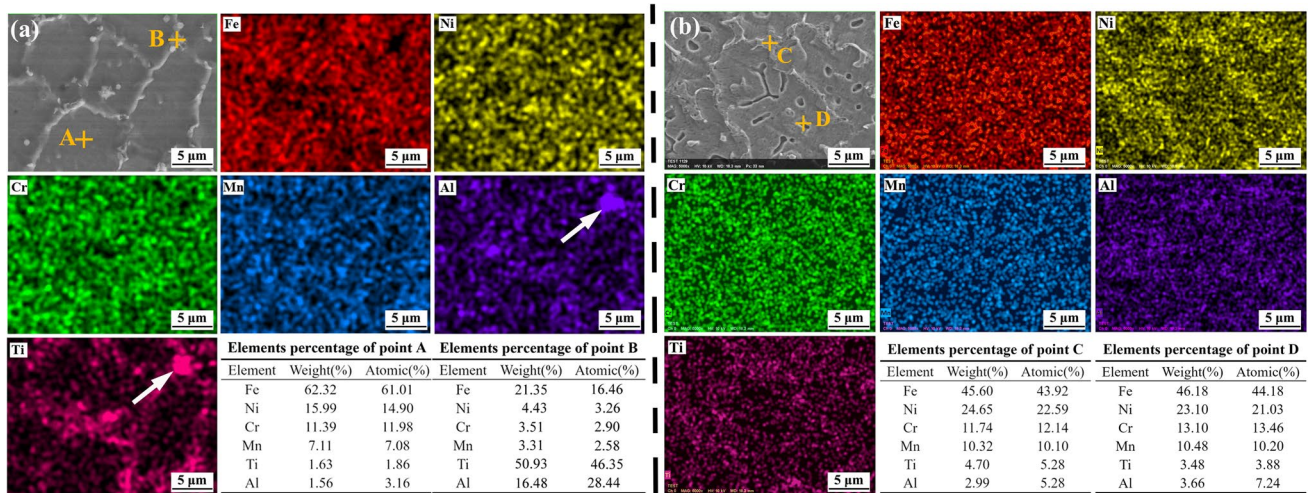


**Fig. 6** Elemental distribution in the WZs of the CrNi<sub>2</sub>MnTi<sub>0.5</sub>Al<sub>0.5</sub> samples: **a** before the PWHT; **b** after the PWHT

found in the matrix for the WZ of the  $\text{CrNi}_2\text{MnTi}_{0.5}\text{Al}_{0.5}$  sample, which deviates from the elemental definition of HEAs. The results may indicate that the weld metal of the  $\text{CrNi}_2\text{MnTi}_{0.5}\text{Al}_{0.5}$  sample may be a type of Fe-based alloy. Compared to the matrix (A-point), the particle (B-point) shows a higher content of Ti and Al elements and a lower content of Fe, Cr, and Ni elements. It confirms that the particles should be Ti–Al-rich particles.

For the  $\text{CrNi}_2\text{MnTi}_{0.5}\text{Al}_{0.5}$  PWHT sample, Fig. 5c and d reveal that the grain morphologies in the WZ are greatly changed compared to the  $\text{CrNi}_2\text{MnTi}_{0.5}\text{Al}_{0.5}$  sample. Columnar grains at the weld edge, as well as equiaxed grains at the weld center, have been transformed into structures with irregular morphologies, including the matrix + convex morphologies. Moreover, the amount of white particles has decreased, but some of them still exist. EDS elemental mapping for the WZ of the  $\text{CrNi}_2\text{MnTi}_{0.5}\text{Al}_{0.5}$  PWHT sample is presented in Fig. 6b. A finding is that the segregation of the Ti element is weakened. The observation indicates that some of those Ti–Al-rich particles in the WZ of the  $\text{CrNi}_2\text{MnTi}_{0.5}\text{Al}_{0.5}$  sample have been dissolved into the matrix during the PWHT process. In addition, EDS point analysis was used to examine the elemental content of the convex structure (C-point) and the matrix (D-point). Only a small difference in the elemental content is observed between C-point and D-point. And the dissolution of particles has increased the content of Ti and Al elements and reduced the relative Fe element content in the matrix. The Fe element content is less than 50 at.% for the  $\text{CrNi}_2\text{MnTi}_{0.5}\text{Al}_{0.5}$  PWHT sample, as shown in Fig. 6b.

Figure 7a presents the XRD patterns of the FeCoCrNiMn samples before and after the PWHT. Only an FCC phase with the diffraction peaks  $2\theta$  of  $43.6^\circ$ ,  $50.5^\circ$ , and

$74.4^\circ$  has been detected. It means that the phase structure for the FeCoCrNiMn sample has not changed during the PWHT. It is in good accordance with previous studies that the FeCoCrNiMn alloy shows good phase stability during the annealing process [48–50]. Nam et al. [35] suggested that only a single FCC phase could be detected in the WZ of the welded joint of FeCoCrNiMn alloy during the PWHT at  $800 \sim 1000^\circ\text{C}$ . For the  $\text{CrNi}_2\text{MnTi}_{0.5}\text{Al}_{0.5}$  samples, the main FCC phase with the diffraction peak  $2\theta$  of  $43.4^\circ$ ,  $50.3^\circ$ , and  $74.0^\circ$  has been detected. The Ti–Al phases have not been detected in the XRD patterns of the  $\text{CrNi}_2\text{MnTi}_{0.5}\text{Al}_{0.5}$  samples. The reason may be related to the low volume content of the particles. Similar to the FeCoCrNiMn samples, the position of diffraction peaks of the  $\text{CrNi}_2\text{MnTi}_{0.5}\text{Al}_{0.5}$  sample has not been changed during the PWHT process.

## 4 Discussion

In multi-principal materials, phase structures have an impact on mechanical properties. And the phase structures in multi-principal materials can be predicted by using some thermodynamic parameters, such as entropy of mixing ( $\Delta S_{\text{mix}}$ ), enthalpy of mixing ( $\Delta H_{\text{mix}}$ ), and atomic size difference ( $\delta$ ) based on previous studies. The calculation of those parameters can be found in equations as follows:

$$\bar{r} = \sum_{i=1}^n c_i r_i \quad (1)$$

$$\delta = \sqrt{\sum_{i=1}^n c_i \left(1 - \frac{r_i}{\bar{r}}\right)^2} \quad (2)$$

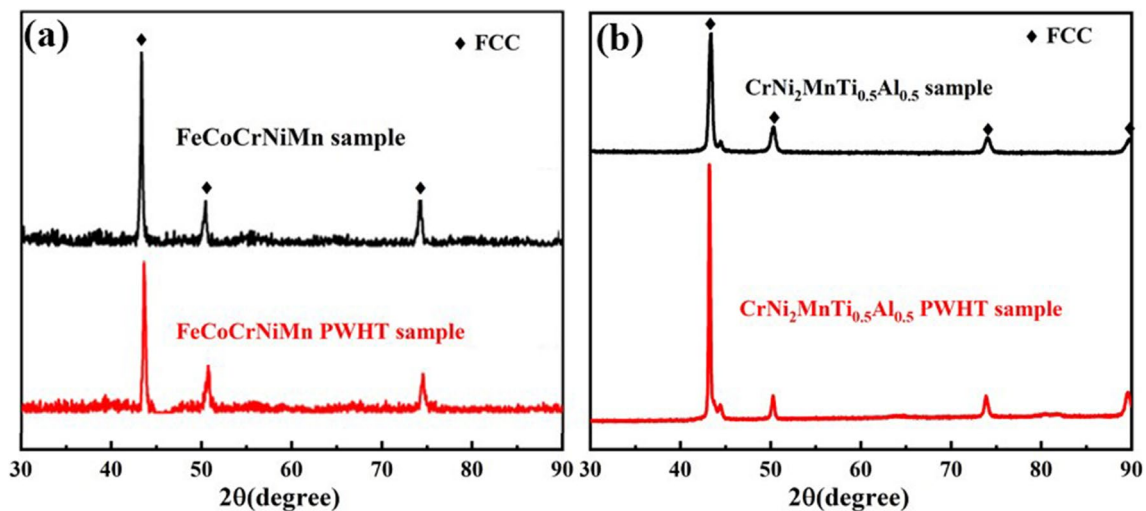


Fig. 7 XRD patterns of the WZs for various samples: **a** FeCoCrNiMn samples; **b**  $\text{CrNi}_2\text{MnTi}_{0.5}\text{Al}_{0.5}$  samples



$$\Delta H_{mix} = \sum_{i=1}^n \Omega_{ij} c_i c_j \tag{3}$$

$$\Delta S_{mix} = -R \sum_{i=1}^n (c_i \ln c_i) \tag{4}$$

Here, the atomic percent and radius of element *i* are represented by *c<sub>i</sub>* and *r<sub>i</sub>*, respectively. The mixing enthalpy between element *i* and element *j* is represented by  $\Omega_{ij}$ . The parameter *R* is the gas constant. Its value is 8.314 J/(mol•K) [51]. It is proposed that a single solid solution phase can be generated at  $-15 \leq \Delta H_{mix} \leq 5$  kJ/mol,  $\delta \leq 4.3$ , and  $12 \leq \Delta S_{mix} \leq 17.5$  J/(mol•K) [52]. And multiphase structures would form in multi-principal alloys under less restricted conditions, which is consistent with  $-22 \leq \Delta H_{mix} \leq 7$  kJ/mol,  $\delta \leq 8.5$ , and  $11 \leq \Delta S_{mix} \leq 19.5$  J/(K•mol) [53]. Furthermore, according to the definition of HEA, the value of  $\Delta S_{mix}$  in the multi-principal materials should be higher than 1.5R [54].

The parameters of  $\Delta S_{mix}$ ,  $\Delta H_{mix}$ , and  $\delta$  are calculated based on the elemental composition shown in Fig. 6. The results in Table 1 show that for the weld center of the FeCoCrNiMn sample, all parameters of  $\Delta S_{mix}$ ,  $\Delta H_{mix}$ , and  $\delta$  can satisfy the requirement of forming a single solid solution phase. In addition to the promising elemental content (5~35 at.%) in the WZ, high-entropy materials with a simple phase structure should be achieved in the FeCoCrNiMn sample. Therefore, no segregation of elements is observed in the WZ of the FeCoCrNiMn sample (Fig. 4f). And, owing to the favorable phase stability of HEAs, the PWHT process has little effect on the phase structures and grain morphologies of the WZ for the FeCoCrNiMn samples. As a result, the tensile properties of the FeCoCrNiMn samples have not deteriorated, and the fracture position for the tensile samples has not changed during the PWHT.

Table 1 shows that for the WZ of the CrNi<sub>2</sub>MnTi<sub>0.5</sub>Al<sub>0.5</sub> sample, the values of  $\Delta S_{mix}$  for the matrix (A-point) and particle (B-point) are lower than 1.5R. It deviates from the definition of HEAs. It means that the value of  $\Delta S_{mix}$  should be higher than 1.5R for HEAs. Therefore, it cannot be considered a high-entropy material. According to the high content of Fe element (see Fig. 6a), the weld metal of the CrNi<sub>2</sub>MnTi<sub>0.5</sub>Al<sub>0.5</sub> sample should be a type of Fe-based alloy. Based on the phase diagram of the Ti–Al binary

alloy, owing to the limited solid solubility between Ti and Al elements, Ti–Al particles such as TiAl, Ti<sub>3</sub>Al, and Al<sub>3</sub>Ti phases could be formed in a high-temperature environment. For the welded joints using CrNi<sub>2</sub>MnTi<sub>0.5</sub>Al<sub>0.5</sub> powders, Ti and Al elements are presented in the molten pool. Therefore, Ti–Al-rich particles have the chance to be formed in the WZ. However, for the CrNi<sub>2</sub>MnTi<sub>0.5</sub>Al<sub>0.5</sub> PWHT sample, the value of  $\Delta S_{mix}$  is significantly increased, compared to the CrNi<sub>2</sub>MnTi<sub>0.5</sub>Al<sub>0.5</sub> sample, and then being higher than 1.5R (see C-point and D-point Table 1). The results imply that the dissolution of Ti–Al enriched particles during the PWHT process can increase the degree of confusion of multi-principal elements in the matrix and increase the value of  $\Delta S_{mix}$ .

Table 1 indicates that the parameters of  $\Delta S_{mix}$ ,  $\Delta H_{mix}$ , and  $\delta$  cannot satisfy the requirement of forming a single solid-solution phase but can meet the condition of forming multiphase structures for the CrNi<sub>2</sub>MnTi<sub>0.5</sub>Al<sub>0.5</sub> sample. Figure 7b indicates that the position of diffraction peaks of the CrNi<sub>2</sub>MnTi<sub>0.5</sub>Al<sub>0.5</sub> sample has not been changed during the PWHT process. However, the thermodynamic parameters, such as  $\Delta S_{mix}$ ,  $\Delta H_{mix}$ , and  $\delta$ , have been significantly changed, which may cause the changes in grain morphologies and mechanical properties of the CrNi<sub>2</sub>MnTi<sub>0.5</sub>Al<sub>0.5</sub> sample (see Figs. 1, 2, and 5). As indicated in Fig. 5, significant changes in grain morphologies in the WZs can be found between the CrNi<sub>2</sub>MnTi<sub>0.5</sub>Al<sub>0.5</sub> and CrNi<sub>2</sub>MnTi<sub>0.5</sub>Al<sub>0.5</sub> PWHT samples. Typical columnar and equiaxed grains are observed in the weld edge and weld center, respectively, for the CrNi<sub>2</sub>MnTi<sub>0.5</sub>Al<sub>0.5</sub> sample. However, after the PWHT, columnar grains in the weld edge, as well as equiaxed grains in the weld center, are less defined. And the structures with irregular morphologies, including the matrix + convex morphologies, are observed. The reason may have a close relationship with the dissolution of particles, as well as the elemental diffusion during the PWHT process. As shown in Fig. 5a and b, many Ti–Al-rich particles in the WZ of the CrNi<sub>2</sub>MnTi<sub>0.5</sub>Al<sub>0.5</sub> sample have been dissolved into the matrix. In addition to the elemental diffusion between the grain boundaries and grain interiors, the difference in elemental content between the grain boundaries and interiors is significantly reduced (Fig. 6). Therefore, the grain boundaries in the CrNi<sub>2</sub>MnTi<sub>0.5</sub>Al<sub>0.5</sub> PWHT samples are less defined. The grain morphologies in the WZ have been transformed into structures with irregular morphologies, including the matrix + convex morphologies (Fig. 5).

**Table 1** The parameters value of  $\delta$ ,  $\Delta S_{mix}$ , and  $\Delta H_{mix}$  for the measured regions of various samples

Samples	Positions	Elemental composition	$\Delta S_{mix}$	$\Delta H_{mix}$	$\delta$
FeCoCrNiMn	Weld center	Fe <sub>25.2</sub> Co <sub>13.3</sub> Cr <sub>23.2</sub> Ni <sub>18.8</sub> Mn <sub>19.5</sub>	13.2	3.79	3.25
CrNi <sub>2</sub> MnTi <sub>0.5</sub> Al <sub>0.5</sub>	A-point	Fe <sub>61</sub> Ni <sub>14.9</sub> Cr <sub>12</sub> Mn <sub>7.1</sub> Ti <sub>1.8</sub> Al <sub>3.2</sub>	10.06	-4.71	3.98
	B-point	Fe <sub>16.5</sub> Ni <sub>3.2</sub> Cr <sub>2.9</sub> Mn <sub>2.6</sub> Ti <sub>46.4</sub> Al <sub>28.4</sub>	10.96	-17.09	6.25
CrNi <sub>2</sub> MnTi <sub>0.5</sub> Al <sub>0.5</sub> PWHT	C-point	Fe <sub>43.9</sub> Ni <sub>22.6</sub> Cr <sub>12</sub> Mn <sub>10.1</sub> Ti <sub>5.3</sub> Al <sub>5.3</sub>	12.54	-9.47	5.33
	D-point	Fe <sub>44.1</sub> Ni <sub>21</sub> Cr <sub>13.5</sub> Mn <sub>10.2</sub> Ti <sub>3.9</sub> Al <sub>7.2</sub>	12.54	-8.97	5.24

Figures 1 and 2 indicate that the PWHT process can significantly increase the hardness in the WZ and rapidly decrease the tensile strength of the CrNi<sub>2</sub>MnTi<sub>0.5</sub>Al<sub>0.5</sub> sample. Based on the above analysis, before the PWHT process, no high-entropy material but a type of Fe-based alloy is formed in the weld metal of the CrNi<sub>2</sub>MnTi<sub>0.5</sub>Al<sub>0.5</sub> sample. The dissolution of Ti–Al enriched particles during the PWHT process causes an increase in the value of  $\Delta S_{\text{mix}}$  and makes the weld metal meet the thermodynamic parameters for forming high-entropy materials. As is known, compared to traditional alloys, HEAs have significant lattice distortion effects, which may cause high hardness and brittle characteristics. Moreover, previous studies indicate that Ti and Al elements have remarkable effects on the mechanical properties of HEAs [55, 56]. Wang et al. [55] reported that increasing the Ti content in FeCoCrNiTi<sub>x</sub> alloys increases the hardness. The hardness value can reach up to 850 HV when  $x = 0.7$ , by accompanying with a huge reduction of ductility. Figure 6 indicates that compared to the CrNi<sub>2</sub>MnTi<sub>0.5</sub>Al<sub>0.5</sub> sample, the content of Ti and Al elements in the weld metal of the CrNi<sub>2</sub>MnTi<sub>0.5</sub>Al<sub>0.5</sub> PWHT sample is increased. Due to the greater atomic radius of Ti and Al elements than other elements, the dissolution of Ti and Al elements may result in severe lattice distortion and solid-solution strengthening in the WZ [55, 56]. As a result, compared to the CrNi<sub>2</sub>MnTi<sub>0.5</sub>Al<sub>0.5</sub> sample, the hardness values of the WZ are sharply increased. Moreover, owing to the melting of BM and weld metal dilution, the chemical composition inhomogeneity and non-uniform microstructure are easily presented in the WZ, which may cause hardness variation in the WZ, especially for the CrNi<sub>2</sub>MnTi<sub>0.5</sub>Al<sub>0.5</sub> PWHT sample (Fig. 1c, d). In addition, the tensile strength and elongation of the CrNi<sub>2</sub>MnTi<sub>0.5</sub>Al<sub>0.5</sub> PWHT sample are significantly decreased compared to the CrNi<sub>2</sub>MnTi<sub>0.5</sub>Al<sub>0.5</sub> sample. The ductility of the weld metal by using CrNi<sub>2</sub>MnTi<sub>0.5</sub>Al<sub>0.5</sub> powders is significantly reduced after the PWHT. Therefore, it appears that there is no requirement for the PWHT process for the welding of 304/Q235 stainless steel composite plate using multi-principal filler materials of FeCoCrNiMn and CrNi<sub>2</sub>MnTi<sub>0.5</sub>Al<sub>0.5</sub>. In summary, the results of this study provide an experimental reference for adjusting the microstructure and mechanical properties of welded joints by using multi-principal filler materials through the PWHT process.

## 5 Conclusions

- (1) A simple phase structure, a face-centered cubic (FCC) phase, was achieved in the weld metal by using FeCoCrNiMn powders. The post-weld heat treatment (PWHT) process had little effect on the grain morphology and phase structure of the weld metal for the FeCoCrNiMn sample.
- (2) For the CrNi<sub>2</sub>MnTi<sub>0.5</sub>Al<sub>0.5</sub> samples, the grain morphologies in the weld zone (WZ) were changed from columnar/equiaxed grains into structures with irregular morphologies during the PWHT process.
- (3) Significant differences in hardness variations were observed in the WZs for the FeCoCrNiMn and CrNi<sub>2</sub>MnTi<sub>0.5</sub>Al<sub>0.5</sub> samples after the PWHT. The hardness of the former was slightly decreased, while that of the latter was sharply increased after the PWHT.
- (4) The PWHT process had a small effect on the tensile properties and fracture position of the FeCoCrNiMn sample. However, the PWHT process had an adverse effect on the tensile properties and fracture position of the CrNi<sub>2</sub>MnTi<sub>0.5</sub>Al<sub>0.5</sub> sample. It significantly decreased the tensile strength and elongation of the CrNi<sub>2</sub>MnTi<sub>0.5</sub>Al<sub>0.5</sub> sample.

**Funding** This study was financially supported by the National Natural Science Foundation of China (52265047), Guangdong Basic and Applied Basic Research Foundation (2022A1515240045).

**Data availability** Research data are not shared.

## Declarations

**Conflict of interest** The authors declare no competing interests.

## References

1. Wu Z, David SA, Leonard DN, Feng Z, Bei H (2018) Microstructures and mechanical properties of a welded CoCrFeMnNi high-entropy alloy. *Sci Technol Weld Joi* 23(7):585–595. <https://doi.org/10.1080/13621718.2018.1430114>
2. Rhode M, Richter T, Schroepfer D, Manzoni AM, Schneider M, Laplanche G (2021) Welding of high-entropy alloys and compositionally complex alloys—an overview. *Weld World* 65(8):1645–1659. <https://doi.org/10.1007/s40194-021-01110-6>
3. Miracle DB, Senkov ON (2017) A critical review of high entropy alloys and related concepts. *Acta Mater* 122:448–511. <https://doi.org/10.1016/j.actamat.2016.08.081>
4. Verma A, Natu H, Balasundar I, Chelvane A, Niranjani VL, Mohape M, Mahanta G, Gowtam S, Shanmugasundaram T (2022) Effect of copper on microstructural evolution and mechanical properties of laser-welded CoCrFeNi high entropy alloy. *Sci Technol Weld Joi* 27(3):197–203. <https://doi.org/10.1080/13621718.2022.2029116>
5. Tsai KY, Tsai MH, Yeh JW (2013) Sluggish diffusion in Co–Cr–Fe–Mn–Ni high-entropy alloys. *Acta Mater* 61(13):4887–4897. <https://doi.org/10.1016/j.actamat.2013.04.058>
6. Li J, Meng X, Wan L, Huang Y (2021) Welding of high entropy alloys: Progresses, challenges and perspectives. *J Manuf Processes* 68:293–331. <https://doi.org/10.1016/j.jmapro.2021.05.042>
7. Nam H, Moon B, Park S, Kim N, Song S, Park N, Na Y, Kang N (2021) Gas tungsten arc weldability of stainless steel 304 using CoCrFeMnNi filler metals for cryogenic applications. *Sci Technol*

- Weld Joi 27(1):33–42. <https://doi.org/10.1080/13621718.2021.1996851>
8. Nam H, Park C, Moon J, Na Y, Kim H, Kang N (2019) Laser weldability of cast and rolled high-entropy alloys for cryogenic applications. *Mater Sci Eng A* 742:224–230. <https://doi.org/10.1016/j.msea.2018.11.009>
  9. Oliveira JP, Curado TM, Zeng Z, Lopes JG, Rossinyol E, Park JM, Schell N, Braz Fernandes FM, Kim HS (2020) Gas tungsten arc welding of as-rolled CrMnFeCoNi high entropy alloy. *Mater Des* 189:108505. <https://doi.org/10.1016/j.matdes.2020.108505>
  10. Shen J, Agrawal P, Rodrigues TA, Lopes JG, Schell N, He J, Zeng Z, Mishra RS, Oliveira JP (2023) Microstructure evolution and mechanical properties in a gas tungsten arc welded Fe<sub>42</sub>Mn<sub>28</sub>Co<sub>10</sub>Cr<sub>15</sub>Si<sub>5</sub> metastable high entropy alloy. *Mater Sci Eng A* 867:144722. <https://doi.org/10.1016/j.msea.2023.144722>
  11. Shen J, Gonçalves R, Choi YT, Lopes JG, Yang J, Schell N, Kim HS, Oliveira JP (2023) Microstructure and mechanical properties of gas metal arc welded CoCrFeMnNi joints using a 308 stainless steel filler metal. *Scr Mater* 222:115053. <https://doi.org/10.1016/j.scriptamat.2022.115053>
  12. Shen J, Agrawal P, Rodrigues TA, Lopes JG, Schell N, Zeng Z, Mishra RS, Oliveira JP (2022) Gas tungsten arc welding of as-cast AlCoCrFeNi<sub>2.1</sub> eutectic high entropy alloy. *Mater Des* 223:111176. <https://doi.org/10.1016/j.matdes.2022.111176>
  13. Shen J, Gonçalves R, Choi YT, Lopes JG, Yang J, Schell N, Kim HS, Oliveira JP (2022) Microstructure and mechanical properties of gas metal arc welded CoCrFeMnNi joints using a 410 stainless steel filler metal. *Mater Sci Eng A* 857:144025. <https://doi.org/10.1016/j.msea.2022.144025>
  14. Martin AC, Oliveira JP, Fink C (2019) Elemental effects on weld cracking susceptibility in Al<sub>x</sub>CoCrCu<sub>y</sub>FeNi high-entropy alloy. *Metall Mater Trans A* 51(2):778–787. <https://doi.org/10.1007/s11661-019-05564-8>
  15. Shen J, Martin AC, Schell N, Fink C, Oliveira JP (2023) Microstructures in arc-welded Al<sub>10</sub>Co<sub>25</sub>Cr<sub>8</sub>Fe<sub>15</sub>Ni<sub>36</sub>Ti<sub>6</sub> and Al<sub>10.87</sub>Co<sub>21.74</sub>Cr<sub>21.74</sub>Cu<sub>21.74</sub>Fe<sub>21.74</sub>Ni<sub>21.74</sub> multi-principal element alloys: comparison between experimental data and thermodynamic predictions. *Mater Today Commun* 34:104784. <https://doi.org/10.1016/j.mtcomm.2022.104784>
  16. Liu D, Wang J, Xu M, Jiao H, Tang Y, Li D, Zhao L, Han S (2020) Evaluation of dissimilar metal joining of aluminum alloy to stainless steel using the filler metals with a high-entropy design. *J Manuf Processes* 58:500–509. <https://doi.org/10.1016/j.jmapro.2020.08.031>
  17. Liu D, Wang W, Zha X, Guo R, Jiao H, Zhao L (2021) Effects of groove on the microstructure and mechanical properties of dissimilar steel welded joints by using high-entropy filler metals. *J Mater Res Technol* 13:173–183. <https://doi.org/10.1016/j.jmrt.2021.04.060>
  18. Liu D, Guo R, Hu Y, Shen M, Tang Y, Zhao L, Li D, Wang X (2019) Dissimilar metal joining of 304 stainless steel to SMA490BW steel using the filler metal powders with a high-entropy design. *Met Mater Int* 26(6):854–866. <https://doi.org/10.1007/s12540-019-00400-5>
  19. Wang W, Liu D, Li B, Li B, Jiao H, Tang Y, Hu Y, Zhao L, Shen M (2022) Evaluation of surface corrosion and wear resistance in the weld metal by using multi-principal filler wires via high-entropy design. *Weld World* 66(11):2389–2402. <https://doi.org/10.1007/s40194-022-01380-8>
  20. Tillmann W, Ulitzka T, Wojarski L, Manka M, Ulitzka H, Wagstyl D (2019) Development of high entropy alloys for brazing applications. *Weld World* 64(1):201–208. <https://doi.org/10.1007/s40194-019-00824-y>
  21. Liu J, Lin D, Hu J, Xi X, Tang Z, Liu Z, Hu S, Bian H, Song X (2022) Microstructure and mechanical properties of a GH3536/SS304 joint brazed with a Co<sub>25</sub>Fe<sub>25</sub>Mn<sub>5</sub>Ni<sub>25</sub>Ti<sub>20</sub> eutectic high-entropy alloy filler. *Mater Charact* 193:112305. <https://doi.org/10.1016/j.matchar.2022.112305>
  22. Hao X, Dong H, Xia Y, Li P (2019) Microstructure and mechanical properties of laser welded TC4 titanium alloy/304 stainless steel joint with (CoCrFeNi)<sub>100-x</sub>Cu<sub>x</sub> high-entropy alloy interlayer. *J Alloys Compd* 803:649–657. <https://doi.org/10.1016/j.jallcom.2019.06.225>
  23. Zheng M, Yang J, Xu J, Jiang J, Zhang H, Oliveira JP, Lv X, Xue J, Li Z (2023) Interfacial microstructure and strengthening mechanism of dissimilar laser al/steel joint via a porous high entropy alloy coating. *J Mater Res Technol* 23:3997–4011. <https://doi.org/10.1016/j.jmrt.2023.02.040>
  24. Bridges D, Zhang S, Lang S, Gao M, Yu Z, Feng Z, Hu A (2018) Laser brazing of a nickel-based superalloy using a Ni-Mn-Fe-Co-Cu high entropy alloy filler metal. *Mater Lett* 215:11–14. <https://doi.org/10.1016/j.matlet.2017.12.003>
  25. Munitz A, Meshi L, Kaufman MJ (2017) Heat treatments' effects on the microstructure and mechanical properties of an equiatomic Al-Cr-Fe-Mn-Ni high entropy alloy. *Mater Sci Eng A* 689:384–394. <https://doi.org/10.1016/j.msea.2017.02.072>
  26. Wang X-G, Li X-G, Yan F-J, Wang C-G (2016) Effect of heat treatment on the interfacial microstructure and properties of Cu-Al joints. *Weld World* 61(1):187–196. <https://doi.org/10.1007/s40194-016-0393-x>
  27. Xia Y, Dong H, Hao X, Li S, Li P, Yang G (2019) Microstructure evolution of TC4 titanium alloy/316L stainless steel dissimilar joint vacuum-brazed with Ti-Zr-Cu amorphous filler metal. *Weld World* 63(2):323–336. <https://doi.org/10.1007/s40194-019-00703-6>
  28. Li Z, Fu L, Zheng H, Yu R, Lv L, Sun Y, Dong X, Shan A (2019) Effect of annealing temperature on microstructure and mechanical properties of a severe cold-rolled FeCoCrNiMn high-entropy alloy. *Metall Mater Trans A* 50(7):3223–3237. <https://doi.org/10.1007/s11661-019-05231-y>
  29. Nong Z-S, Zhang Z-P, Wang H-N, Deng X-G (2019) Microstructure inhomogeneity of as-cast high-entropy alloy and heat treatment improvement. *Mater Sci Technol* 35(14):1749–1755. <https://doi.org/10.1080/02670836.2019.1647383>
  30. Pickering EJ, Muñoz-Moreno R, Stone HJ, Jones NG (2016) Precipitation in the equiatomic high-entropy alloy CrMnFeCoNi. *Scr Mater* 113:106–109. <https://doi.org/10.1016/j.scriptamat.2015.10.025>
  31. Li S, Li J, Shi J, Du Y, Peng Y, Jin F, Xiong J, Zhang F (2021) Microstructure and mechanical properties of the brazed region in the AlCoCrFeNi high-entropy alloy and FGH98 superalloy joint. *Mater Sci Eng A* 804:140714. <https://doi.org/10.1016/j.msea.2020.140714>
  32. Tong Z, Ren X, Jiao J, Zhou W, Ren Y, Ye Y, Larson EA, Gu J (2019) Laser additive manufacturing of FeCrCoMnNi high-entropy alloy: effect of heat treatment on microstructure, residual stress and mechanical property. *J Alloys Compd* 785:1144–1159. <https://doi.org/10.1016/j.jallcom.2019.01.213>
  33. Shabani A, Toroghinejad MR, Shafyei A, Logé RE (2019) Evaluation of the mechanical properties of the heat treated FeCrCuMnNi high entropy alloy. *Mater Chem Phys* 221:68–77. <https://doi.org/10.1016/j.matchemphys.2018.09.033>
  34. Cakmak G (2017) Effect of heat treatment on the microstructure, phase distribution, and mechanical properties of AlCoCuFeMnNi high entropy alloy. *Adv Mater Sci Eng* 2017:1950196. <https://doi.org/10.1155/2017/1950196>
  35. Nam H, Park C, Kim C, Kim H, Kang N (2017) Effect of post weld heat treatment on weldability of high entropy alloy welds. *Sci Technol Weld Joi* 23(5):420–427. <https://doi.org/10.1080/13621718.2017.1405564>
  36. Otto F, Dlouhý A, Pradeep KG, Kuběnová M, Raabe D, Eggeler G, George EP (2016) Decomposition of the single-phase

- high-entropy alloy CrMnFeCoNi after prolonged anneals at intermediate temperatures. *Acta Mater* 112:40–52. <https://doi.org/10.1016/j.actamat.2016.04.005>
37. Sun G, Zhou R, Lu J, Mazumder J (2015) Evaluation of defect density, microstructure, residual stress, elastic modulus, hardness and strength of laser-deposited AISI 4340 steel. *Acta Mater* 84:172–189. <https://doi.org/10.1016/j.actamat.2014.09.028>
  38. Xu XD, Liu P, Guo S, Hirata A, Fujita T, Nieh TG, Liu CT, Chen MW (2015) Nanoscale phase separation in a fcc-based CoCrCuFeNiAl<sub>0.5</sub> high-entropy alloy. *Acta Mater* 84:145–152. <https://doi.org/10.1016/j.actamat.2014.10.033>
  39. Fu J, Cao C, Tong W, Peng L (2018) Effect of thermomechanical processing on microstructure and mechanical properties of CoCrFeNiMn high entropy alloy. *T Nonferr Metal Soc* 28(5):931–938. [https://doi.org/10.1016/s1003-6326\(18\)64727-2](https://doi.org/10.1016/s1003-6326(18)64727-2)
  40. Zhou Z, L othman J (2016) Dissimilar welding of super-duplex and super-austenitic stainless steels. *Weld World* 61(1):21–33. <https://doi.org/10.1007/s40194-016-0408-7>
  41. Ng C, Guo S, Luan J, Wang Q, Lu J, Shi S, Liu CT (2014) Phase stability and tensile properties of Co-free Al<sub>0.5</sub>CrCuFeNi<sub>2</sub> high-entropy alloys. *J Alloys Compd* 584:530–537. <https://doi.org/10.1016/j.jallcom.2013.09.105>
  42. Kim JH, Lim KR, Won JW, Na YS, Kim H-S (2018) Mechanical properties and deformation twinning behavior of as-cast CoCrFeMnNi high-entropy alloy at low and high temperatures. *Mater Sci Eng A* 712:108–113. <https://doi.org/10.1016/j.msea.2017.11.081>
  43. Dinda GP, Dasgupta AK, Mazumder J (2009) Laser aided direct metal deposition of Inconel 625 superalloy: microstructural evolution and thermal stability. *Mater Sci Eng A* 509(1–2):98–104. <https://doi.org/10.1016/j.msea.2009.01.009>
  44. Gu D, Shi Q, Lin K, Xi L (2018) Microstructure and performance evolution and underlying thermal mechanisms of Ni-based parts fabricated by selective laser melting. *Addit Manuf* 22:265–278. <https://doi.org/10.1016/j.addma.2018.05.019>
  45. Xia H, Li L, Tan C, Yang J, Li H, Song W, Zhang K, Wang Q, Ma N (2022) In situ SEM study on tensile fractured behavior of Al/steel laser welding-brazing interface. *Mater Des* 224:111320. <https://doi.org/10.1016/j.matdes.2022.111320>
  46. Guo Y, Wu Y, Zhang W, Xu M, Li L, Wu Z (2021) Investigation on microstructure and properties of dissimilar joint between TRIP800 and QP980 fabricated by laser welding. *Sci Technol Weld Joi* 26(2):161–172. <https://doi.org/10.1080/13621718.2020.1868700>
  47. Jin Y, Su J, Gao C, Zhao Y, Liu H, Oliveira JP, Tan C, Yu Z (2021) Effect of heat input on interfacial microstructure, tensile and bending properties of dissimilar Al/steel lap joints by laser welding-brazing. *Opt Laser Technol* 142:107218. <https://doi.org/10.1016/j.optlastec.2021.107218>
  48. Li C, White R, Fang XY, Weaver M, Guo YB (2017) Microstructure evolution characteristics of Inconel 625 alloy from selective laser melting to heat treatment. *Mater Sci Eng A* 705:20–31. <https://doi.org/10.1016/j.msea.2017.08.058>
  49. Chang SY, Li CE, Huang YC, Hsu HF, Yeh JW, Lin SJ (2014) Structural and thermodynamic factors of suppressed interdiffusion kinetics in multi-component high-entropy materials. *Sci Rep* 4:4162. <https://doi.org/10.1038/srep04162>
  50. Fiochi J, Casati R, Tuissi A, Biffi CA (2022) Laser beam welding of CoCuFeMnNi high entropy alloy: processing, microstructure, and mechanical properties. *Adv Eng Mater* 24(10):2200623. <https://doi.org/10.1002/adem.202200523>
  51. Liu D, Zha X, Wang W, Tang Y, Jiao H, Hu Y, Zhao L, Zhang J (2022) Microstructure and mechanical properties of welded joints of stainless steel clad sheets using Cr-Ni-Cu-Al multi-principal filler wires. *J Mater Eng Perform*. <https://doi.org/10.1007/s11665-022-07257-7>
  52. Zhang Y, Zhou YJ, Lin JP, Chen GL, Liaw PK (2008) Solid-solution phase formation rules for multi-component alloys. *Adv Eng Mater* 10(6):534–538. <https://doi.org/10.1002/adem.20070240>
  53. Tsai M-H, Yeh J-W (2014) High-entropy alloys: a critical review. *Mater Res Lett* 2(3):107–123. <https://doi.org/10.1080/21663831.2014.912690>
  54. Ye YF, Wang Q, Lu J, Liu CT, Yang Y (2015) Design of high entropy alloys: a single-parameter thermodynamic rule. *Scr Mater* 104:53–55. <https://doi.org/10.1016/j.scriptamat.2015.03.023>
  55. Wang X, Liu Q, Huang Y, Xie L, Xu Q, Zhao T (2020) Effect of Ti content on the microstructure and corrosion resistance of CoCrFeNiTi<sub>(x)</sub> high entropy Alloys prepared by laser cladding. *Materials* 13(10):2209. <https://doi.org/10.3390/ma13102209>
  56. Chen X, Yan L, Karnati S, Zhang Y, Liou F (2017) Fabrication and characterization of Al<sub>x</sub>CoFeNiCu<sub>1-x</sub> high entropy alloys by laser metal deposition. *Coatings* 7(4):47. <https://doi.org/10.3390/coatings7040047>

**Publisher's note** Springer Nature remains neutral with regard to jurisdictional claims in published maps and institutional affiliations.

Springer Nature or its licensor (e.g. a society or other partner) holds exclusive rights to this article under a publishing agreement with the author(s) or other rightsholder(s); author self-archiving of the accepted manuscript version of this article is solely governed by the terms of such publishing agreement and applicable law.